

Microstructure and Mechanical Properties of Friction Stir Process Derived Al-TiO₂ Nanocomposite

H.C. Madhu , P. Ajay Kumar, Chandra S. Perugu, and Satish V. Kailas

(Submitted October 12, 2017; published online January 29, 2018)

Aluminum-based composites have many advantages over their conventional counterparts. A major problem in such composites is the clustering of particles in the matrix. Friction stir processing (FSP) can homogenize particle distribution in aluminum-based composites. In this study, unannealed TiO₂ particles were used to prepare Al-TiO₂ nanocomposite using FSP. The TiO₂ particles, about 1 μm, were dispersed into an aluminum matrix by 6 passes of FSP. The TiO₂ particles were fractured by multiple FSP passes, leading to a nano-size particle distribution in the matrix. Nanoscale dispersion was confirmed by scanning electron microscopy and transmission electron microscopy. The fractured TiO₂ particles reacted with the aluminum matrix to form Al₃Ti intermetallic and Al₂O₃ ceramic. The progression of the Al-TiO₂ reaction from the fourth to the sixth pass of FSP was revealed by x-ray diffraction. Due to the nanoscale dispersion, the yield and ultimate tensile strength of the composite increased to 97 and 145 MPa, respectively. Ductility of the composite decreased marginally compared to the as-received aluminum. As the dispersed particles pin dislocations, the strain-hardening rate of the composite was considerably increased and the same was seen in the Kocks-Mecking plot. The TiO₂ particles are mechanically activated due to their fracture during FSP, hence leading to reaction with the matrix. The particle refinement and dispersion lead to a homogeneous matrix with higher strength.

Keywords friction stir processing (FSP), metal matrix composites, nanoparticles, titanium dioxide

1. Introduction

Friction stir welding (FSW), a solid-state joining process developed by the Welding Institute in Cambridge, England (Ref 1), has emerged as the method to join all aluminum alloys. In FSW, a nonconsumable rotating tool, with a specially designed pin and shoulder, is plunged into the interface between the two plates and traversed along the joint line. The workpiece is plasticized due to localized heating by the rotating tool. As the tool traverses along the joint line, the soft metal is extruded around the tool pin before being forged by the downward pressure applied by the tool shoulder (Ref 2). FSW can join dissimilar metals with widely varying melting points and hardness (Ref 3). FSW has been used to weld composites (Ref 4, 5). Based on the principle of FSW, Mishra et al. (Ref 6) developed friction stir processing (FSP) for microstructural refinement of materials (Ref 7-10). FSP is a potential tool for many applications which include (a) formation of ultrafine grains in aluminum alloys that exhibit superplasticity (Ref 6, 11-13), (b) homogenization of agglomerated aluminum nanocomposites (Ref 14), (c) synthesis of aluminum compos-

ites (Ref 15, 16) and (d) fabrication of a surface composite (Ref 17). Recently, FSP successfully produced an ultrafine-grained Al-Al₂Cu in situ composite from an Al-Cu elemental powder mixture (Ref 18) and Al-Al₃Ti nanocomposites (Ref 19).

Aluminum-based composites reinforced with hard ceramic particles have received considerable interest because of their high specific strength, stiffness and resistance to wear. Aluminum matrix composites (AMCs) have potential applications in automotive, aeronautical and aerospace industries. Therefore, simple and economical methods for fabricating AMCs are a sought-after research area. Strengthening mechanisms in the composites can be classified into direct and indirect strengthening (Ref 20). Direct strengthening occurs when loads are transferred from the weak matrix to the hard reinforcements (Ref 20, 21), while indirect strengthening results from the change in the matrix microstructure (for example, the Orowan strengthening mechanism, grain refinement, dislocation multiplication) of the composites because of the reinforcements (Ref 22-24). In metal matrix composites (MMC's), damage evolution starts, preferentially, in the particle. This is because of the particle agglomeration leading to stress triaxiality, due to which, problems such as accelerated fatigue life, lower impact resistance and ductility, along with the poor predictability of properties of MMCs have been the major issues that have limited their use. To overcome these drawbacks, use of nanoparticles has been attracting attention in composite research. The ability of nanoparticles in improving mechanical and physical properties of MMCs is the reason for increasing attention in this direction. To realize the full potential of the nanoparticles, a nanoscale dispersion is essential. With the nanoscale dispersion, problems related to fatigue, fracture toughness and creep can be greatly alleviated. However, manufacturing costs and environmental concerns need to be addressed.

Nano-MMCs have been produced through the powder metallurgy route (Ref 25). Secondary processing, such as

H.C. Madhu and Satish V. Kailas, Department of Mechanical Engineering, Indian Institute of Science, Bengaluru 560012, India; P. Ajay Kumar, Department of Materials Science and Engineering, University of Wisconsin Milwaukee, Milwaukee, WI; and Chandra S. Perugu, Department of Materials Engineering, Indian Institute of Science, Bengaluru 560012, India. Contact e-mail: hcmadhu@gmail.com.

extrusion and rolling, is often needed to consolidate materials produced by this route. An alternative route is to introduce ceramic particles by stirring them into molten metal (Ref 26). However, the nanoparticles form hard agglomerates that are difficult to disperse through physical mixing (Ref 27).

FSP has successfully evolved into a method to fabricate MMCs, which are environmentally friendly and economical in terms of time and cost. During the past decade, a large number of investigations have been carried out to process MMCs by FSP. In an earlier study on the in situ FSP Al-TiO₂ composite, a mixture of Al and TiO₂ powders was sintered, forged and followed by FSP (Ref 28). Khodabakhshi et al. (Ref 29) directly incorporated TiO₂ particles in the Al5052 alloy; however, there was no significant increase in strength, and a considerable loss in ductility was observed. In another study, Al-Mg alloy composites were prepared with a varying volume fraction of TiO₂ (Ref 30). In the study, for a volume fraction of six percent, TiO₂ was unevenly distributed even after 12 passes of FSP. It was also reported that for an optimum volume fraction of three percent, the ultimate tensile strength increased by 40% and the ductility was reduced by 56%. The reaction products of TiO₂ and the matrix have been evaluated with elemental mapping in SEM and TEM. Visweswara et al. (Ref 31) have incorporated TiO₂ by FSP to evaluate the anodizing behavior and optical appearance. To the best of the author's knowledge, there is no report about the effect of successive FSP passes on Al-TiO₂ reaction.

The objective of the present study is to fabricate a fully dense Al-TiO₂ nanocomposite without any pre- or post-processing. Unannealed TiO₂ particles were incorporated into the aluminum matrix by FSP. A detailed characterization of the microstructural and mechanical properties of the Al-TiO₂ composite was carried out. The evidence of particle refinement by fracture, which leads to the reaction of Al-TiO₂, is also presented. The reaction of TiO₂ with aluminum during successive passes of FSP was characterized using x-ray diffraction.

2. Experimental

Titanium isopropoxide, commonly referred to as titanium tetra-isopropoxide (TTIP), with the chemical formula Ti{OCH(CH₃)₂}₄ and the structure shown in Fig. 1(a), was used as a precursor to synthesize TiO₂ in this study. The TTIP precursor of 5 ml was mixed with 15 ml isopropanol. This solution was slowly added to 250 ml of distilled water. The solution was maintained at a pH of 7 to 10 by adding either HNO₃ or NH₄OH. This mixture was heated to 60°C (± 10°C) and vigorously stirred to cause gelation. A bluish-white gel of about 50 ml was obtained after 18-20 h. The gel was washed with ethanol and dried at 100°C in a vacuum; after 3 h, a yellowish-white powder had formed (Ref 32). The particles of the powder were 1 μm in size and were measured by dynamic light scattering (DLS). To confirm that the particles were of TiO₂, energy dispersive spectroscopy (EDS) on SEM (Sirion, Model VL 30FEG) to find elements was done (Fig. 1c). Then, the phases present were confirmed by x-ray diffraction (XRD) studies conducted on a PANalytical (JDX-8030) using a Cu-Kα radiation. The XRD of the amorphous powder revealed a broad pattern of an anatase phase with low-intensity brookite phase (Fig. 1d).

In the present work, commercially pure (CP) aluminum (99.5%) plates of 6 mm thickness, 200 mm long and 80 mm wide were used as matrix material. On these plates, grooves of 160 mm length, 3 mm width and 4 mm depth were machined. These grooves were filled with TiO₂ particles and sealed with CP aluminum strips of 2 mm thickness. A high carbon steel tool with a shoulder diameter of 25 mm, and an 8 to 6 mm diameter conical pin with a thread of 1 mm pitch and a pin height of 5 mm were used. All the experiments were done on a five-axis friction stir welding machine (Make: BISS-ITW, Bangalore). The experiments were done at a tool rotation speed of 1200 rpm, traverse speed of 25 mm/min and a tool tilt of 2°. The rotating tool traversed the sealed groove of the workpiece. The tool traversed the same path up to 6 times. The workpiece was cooled to room temperature between each pass of the tool. For comparison, a CP aluminum plate was processed with six FSP passes without reinforcement under identical parameters.

The samples of as-received CP aluminum, FSPed CP aluminum and the synthesized composite were cut in a direction perpendicular to the tool traverse. The samples were carefully ground on SiC abrasive papers from 400 to 3000 grit. Then, the samples were polished with an alumina slurry and, finally, with a diamond paste of 1-2 μm particle size. To remove dust/abrasive particles, the samples were cleaned ultrasonically. All the samples were etched with freshly prepared Kroll's reagent. For EBSD, the samples were electropolished using A2 electrolyte. Macro-images from the sample were captured on a stereo microscope. The samples were also characterized using a SEM (ESEM Quanta200, Make: FEI) and a TEM (TEC-NAI F30). The size, distribution and volume fraction of the TiO₂ particles were measured using image analysis software ImageJ. Tensile samples were machined from the processed zone using a wire electric discharge machine, and the schematics of the location and dimensions were as shown in Fig. 2. Tensile tests were carried out on an Instron UTM at a strain rate of 10⁻³ s⁻¹.

3. Results

3.1 Microstructures and Phase Analysis

The macroscopic images in Fig. 3(a), (b), (c), (d), (e), and (f) show the cross section of the processed composite from first pass to sixth pass. After first pass, the composite shows particle agglomeration near the top of the nugget below the shoulder effected region (Fig. 3a). The agglomeration is discontinuous and extends from advancing side (AS) to the retreating side (RS). The second pass also shows similar discontinuous agglomeration extending from AS to RS, but the area is reduced (Fig. 3b). After third pass, the agglomerations are concentrated in AS but are still discrete (Fig. 3c). At the end of the fourth pass, discrete agglomerations are merged and located toward AS (Fig. 3d). After the fifth pass, the composite shows as marked reduction in agglomerated area and except on the AS, particles are evenly distributed in the nugget (Fig. 3e). The six pass sample shows a nugget without any macroscopic agglomeration, and the boundary between the stir zone and the base metal is clearly defined (Fig. 3f). The processed zone of the sample was about 8 mm wide and 5 mm thick.

The diffraction patterns of the four, fifth and sixth pass samples show that the intensity of the TiO₂ reduced and Al₂O₃

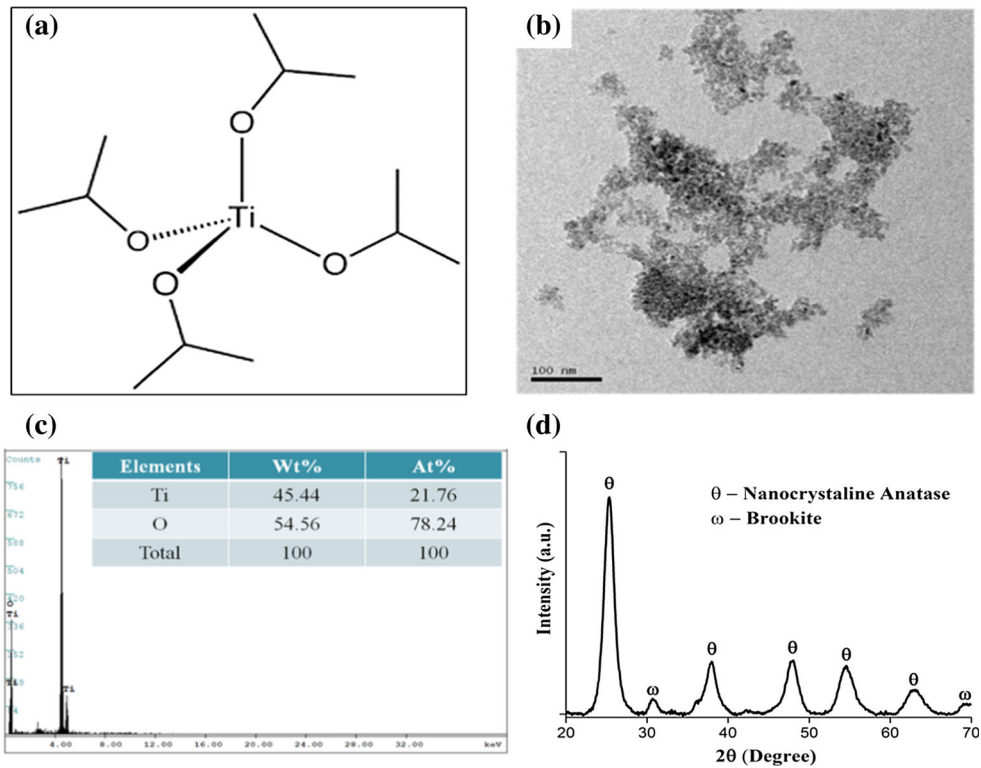


Fig. 1 (a) The structure of titanium tetra-isopropoxide(TTIP) (b) TEM image of TiO_2 powder (c) EDS elemental analysis of TiO_2 powder and (d) x-ray diffraction confirms nanocrystalline TiO_2 phase

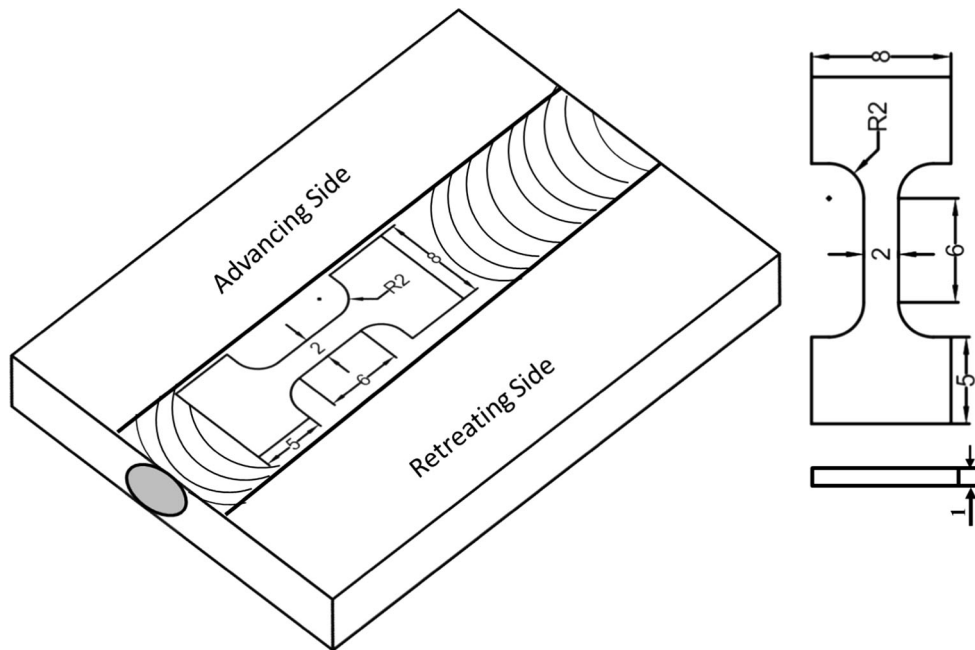


Fig. 2 Schematic diagram of FSPed plate and tensile test specimen

increased (Fig. 4). As shown in from the reaction (1), TiO_2 is reduces to form Al_3Ti and Al_2O_3 . From the XRD and reactions, it can be stated that the reaction of TiO_2 with the aluminum matrix is aided by FSP. With each pass of FSP, the particles are refined. As smaller particles have higher surface energy, the

activation energy tends to reduce. As the activation energy is reduced, the TiO_2 reaction with aluminum proceeds at a lower temperature during FSP. The residual peaks of TiO_2 in Fig. 4 indicate an incomplete reaction, which is due to larger TiO_2 particles whose activation energies remain large.

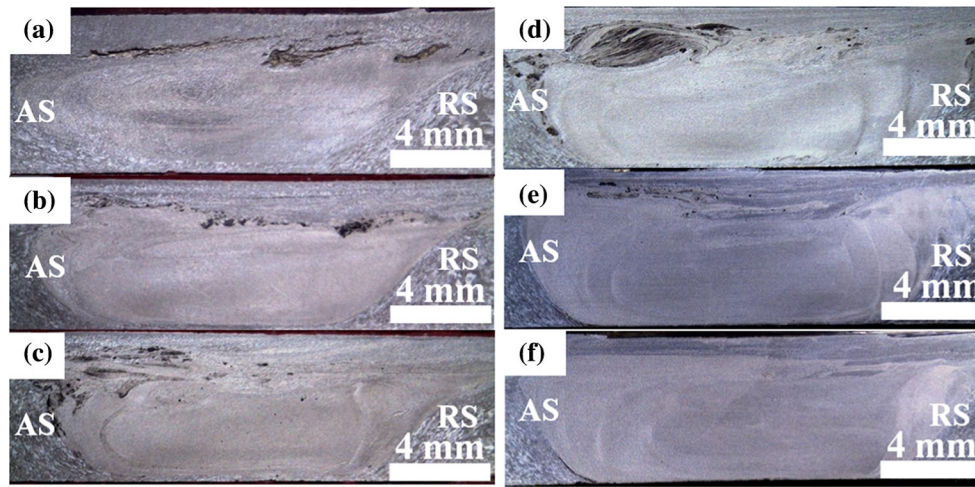


Fig. 3 Stereo macrographs of the FSPed Al-TiO₂ composites after (a) pass 1 (b) pass 2 (c) pass 3 (d) pass 4 (e) pass 5 and (f) pass 6

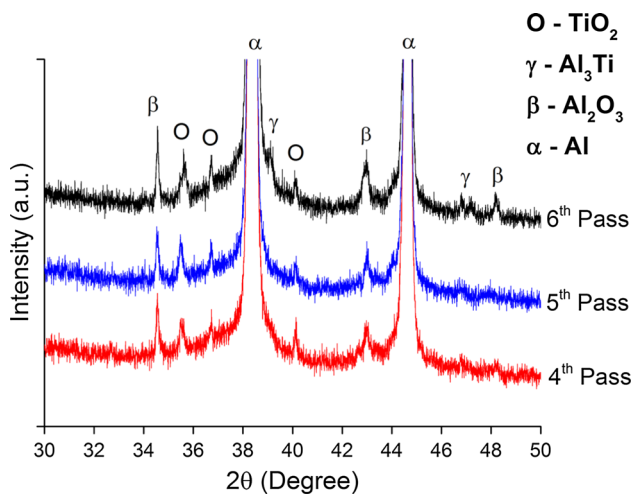
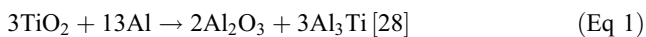


Fig. 4 X-ray diffraction pattern showing reduction in TiO₂ intensity with increasing the number of FSP passes



The grains of as-received CP aluminum were refined from 50 μm to about 5 μm in the Al-TiO₂ composite shown in Fig. 5(a) and (b). EBSD (inverse pole figure + grain boundaries) map of the processed Al-TiO₂ composite is shown in Fig. 5c. The reinforcement particles are not indexed; hence, they are seen as black particles. The grain size refinement in the composite was due to combined effect of dynamic recrystallization and presence of secondary particles, which increased the nucleation sites, consequently reduced the grain size of the aluminum matrix during FSP (Ref 33, 34). The TEM image of the FSP composite also shows the sub-grain structure pinned by nanoparticles (Fig. 5d). Figure 6 shows that the particle sizes are distributed from submicron to a few microns. The larger particles are suspected to be of un-reacted TiO₂.

Further, to understand the particle refinement and the reaction mechanism of Al-TiO₂ composites during FSP, a TEM analysis was carried out with emphasis on particle fracture. The observed

images contain particles with pores and cracks as shown in Fig. 7(a) and (b). Figure 7(a), (b), (c), (d) and (e) shows the fracture mechanism of the particle during FSP. Large particles (Fig. 7a) with pores and cracks (Fig. 7b and c) are fractured due to the stirring action of the tool pin, leading to finer particles (Fig. 7d and e). Porous particles have low fracture toughness; hence, they are easily fractured to the nanoscale by successive FSP passes. Due to this particle refinement the surface energy of the particle increases, and this, in turn, reduces the activation energy of Al-TiO₂ reaction. The TEM analysis also confirmed the nanoscale dispersion of particles as shown in Fig. 8(a). The dispersed particles were identified as Al₃Ti based on the selected area electron diffraction (SAED) patterns and the EDS analysis (Fig. 8a and b).

3.2 Tensile Behavior

Figure 9 shows the room-temperature engineering stress-strain curves of as-received, sixth pass FSPed CP aluminum and the FSP synthesized Al-TiO₂ composite. The tensile test results of the as-received sixth pass FSPed CP aluminum and Al-TiO₂ composite are given in Table 1. From the tensile test data in Table 1, the sixth pass FSPed aluminum showed a yield strength of 76 ± 4 MPa, an ultimate tensile strength of 111 ± 6 MPa and a 36% elongation, and the increase in strength is attributed due to the grain refinement during FSP. In this case, Al-TiO₂ composite yield strength (97 ± 1 MPa) and ultimate tensile strength (145 ± 3 MPa) of the composite increased by 26 and 44% and ductility of the composite decreased to 34% from 37%, compared to as-received CP aluminum. Figure 10(a) and (b) shows fractographs of as-received aluminum and Al-TiO₂ composite samples. While both samples show a ductile fracture, in the case of the Al-TiO₂ composite, two different sizes of dimples were observed. Most of the dimples contain fractured particles, indicating good interfacial bonding with the matrix. The fractured particles suggest that cracks had nucleated in the particle (Fig. 10b). Two types of particles were observed in the fractographs, large fractured particles, and smaller particles without cracks. This indicates that fracture starts at the large TiO₂ (un-reacted) particles.

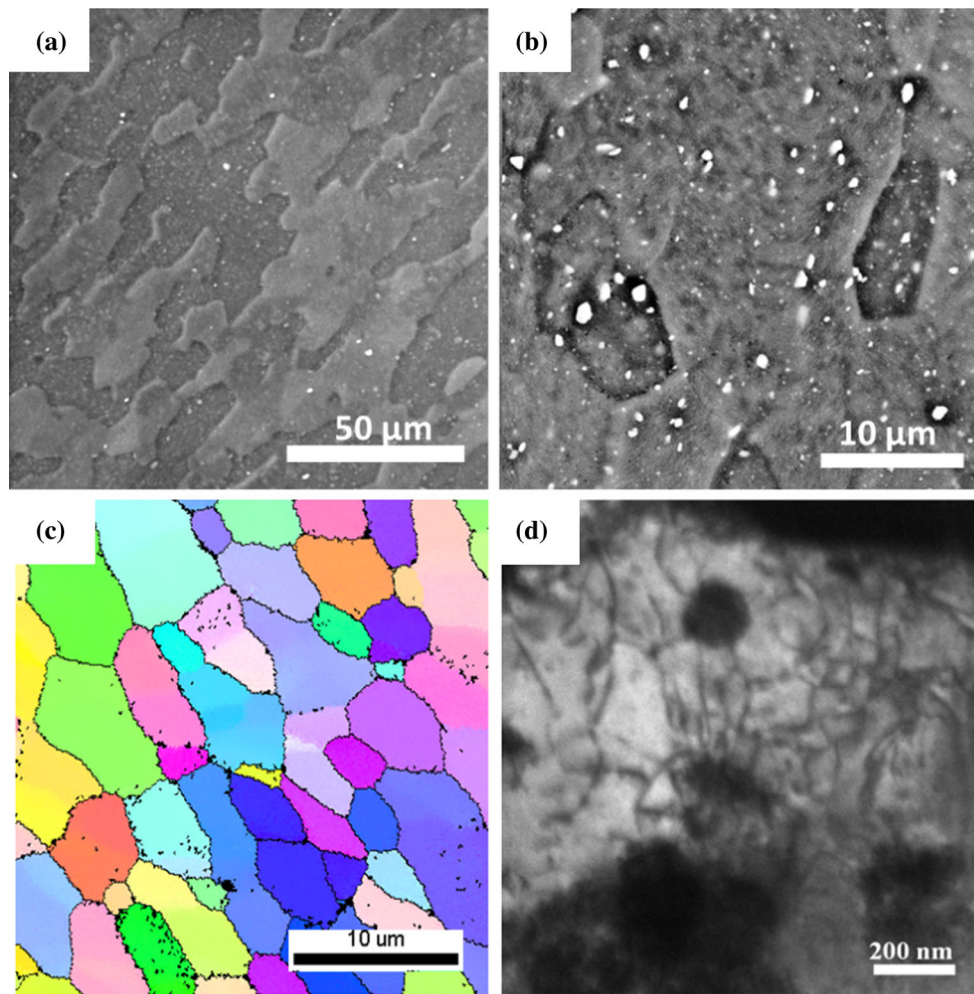


Fig. 5 SEM micrograph shows (a) as-received CP Al, (b) sixth pass FSP processed Al-TiO₂ composite, (c) EBSD-IPF map of the composite and (d) TEM bright field image shows the sub-grain formation after sixth pass FSPed Al-TiO₂ composite

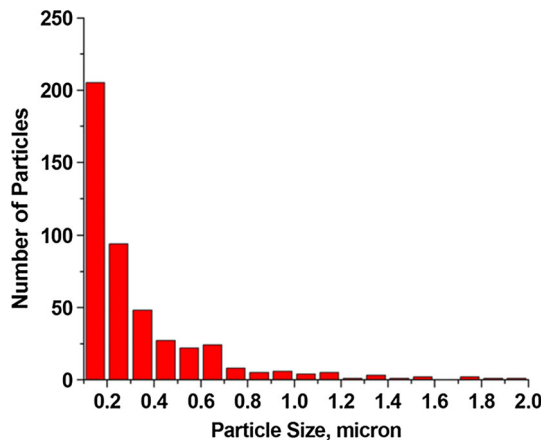


Fig. 6 Particle size distribution of FSPed Al-TiO₂ composite after sixth pass

4. Discussion

The combination of large stresses and heating during multi-pass FSP was responsible for the synthesis of the nanocomposite in this study. Due to frictional heating between the tool and the

workpiece, the workpiece was severely deformed in a localized area (Ref 2). The agglomerated particles were stretched along the shear stress directions, which lead to particle distribution and fragmentation (Ref 35). Multi-pass stirring caused a high plastic strain (Ref 36), which resulted in the homogeneous distribution of the TiO₂ particles in the matrix.

Strengthening in the stir zone is due to a combination of recrystallization and dispersion of nanoparticles in the matrix (Ref 35-37). Strengthening depends on dislocation interaction in the metallic materials. Any obstacle to dislocation movement leads to strengthening of the matrix. Hence, a uniform distribution of nanoparticles will affect the dislocation mobility and may lead to their multiplication. Strengthening of the Al-TiO₂ composite is also due to dislocation interaction with the nanoparticles. Figure 11(a) shows dislocation movement impeded due to entanglement around the particles, and Figure 11(b) shows dislocations pinned by the nanoparticles. It is also seen that the particles have pinned the grain boundary (Fig. 11c). The particles at grain boundary retard the grain growth by pinning the grain boundaries and hence arrest the grain growth (Ref 38). The pinning of second-phase particles on grain boundaries is called Zener pinning. Assuming a uniform distribution of particles, the Zener limiting grain size (d_z) can be calculated using Eq 2:

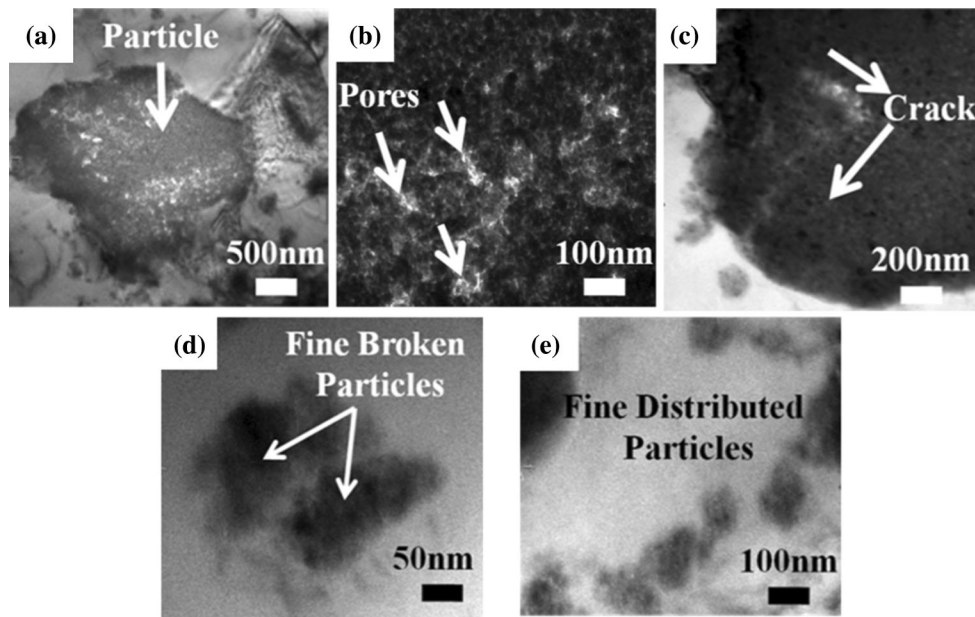


Fig. 7 TEM micrograph shows the fracture mechanism of TiO₂ particle during FSP

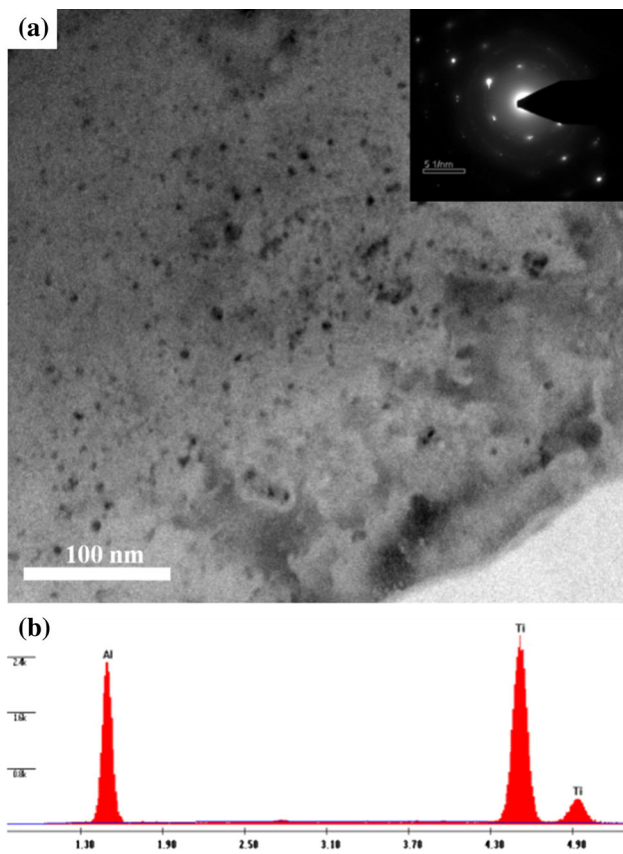


Fig. 8 TEM bright field image showing (a) uniform dispersion of nanoparticles in the aluminum matrix and (b) EDS elemental analysis

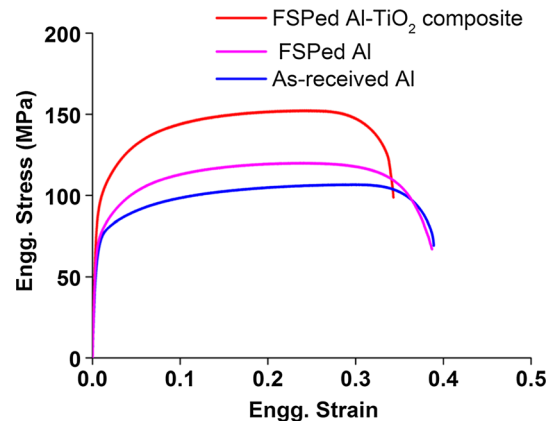


Fig. 9 Comparison of engineering stress vs. engineering strain curve of as-received CP Al, sixth pass FSPed Al and Al-TiO₂ composite

$$d_z = \frac{4r}{3V_f} \quad (\text{Eq 2})$$

where r and V_f are the radius and volume fraction of the particles, respectively (Ref 38). Average particle size and volume fraction of the composite (as calculated from image analysis software ImageJ) were 0.38 μm and 6.7%, respectively. Calculated Zener limiting grain size was around 4 μm , and the actual grain size was found to be 5 μm ; this suggests that the grain growth in the composite is controlled by the Zener pinning pressure.

Assuming Al-TiO₂ is an isotropic composite, with a volume fraction of 6.7%, from the Orowan-Ashby equation the net change in the yield strength can be calculated (Eq 3).

Table 1 Tensile properties of as-received Al, FSP Al and Al-TiO₂ composite samples

Sample	YS, MPa	UTS, MPa	% Elongation
As-received CP Al	77 ± 5	102 ± 4	37 ± 2
sixth pass FSPed CP Al	76 ± 4	111 ± 6	36 ± 2
Al-TiO ₂ Composites	97 ± 1	145 ± 3	34 ± 1

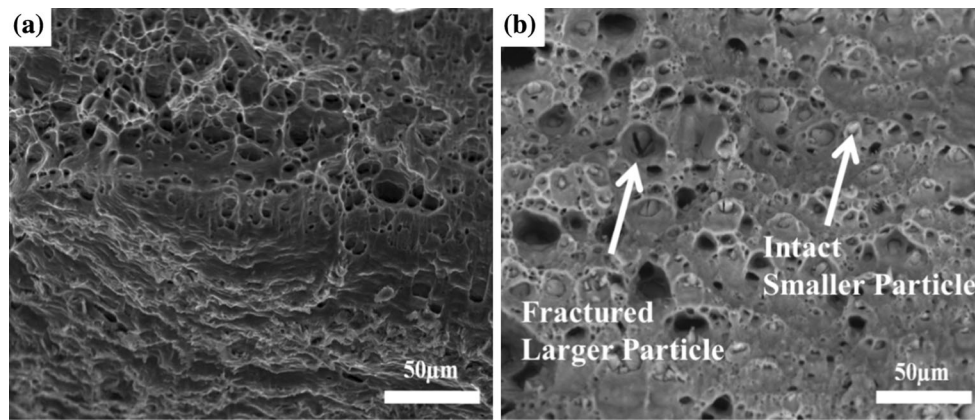


Fig. 10 SEM micrographs show the Fractography of the as-received CP Al and Al-TiO₂ composite after sixth pass FSP

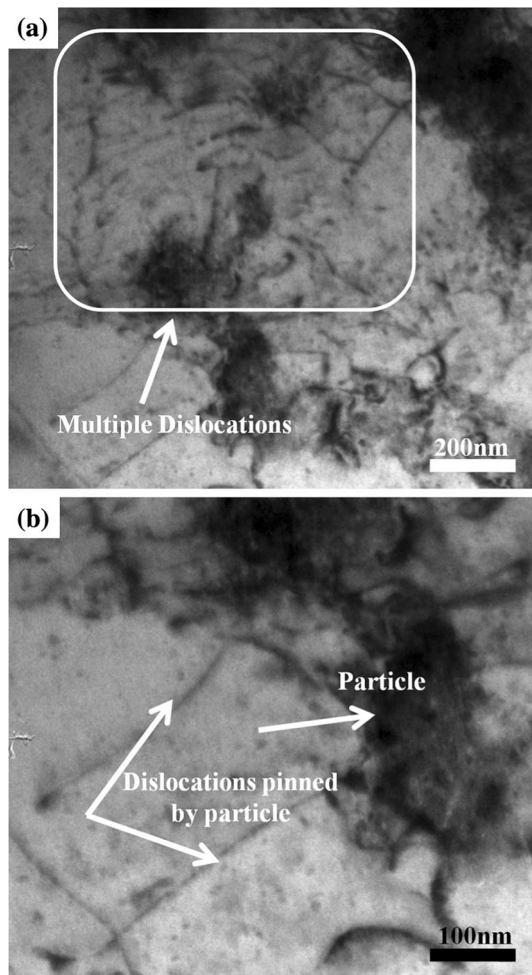


Fig. 11 TEM bright field image of Al-TiO₂ composite after FSP shows (a) dislocation multiplication around the particle and (b) dislocations pinned by the particle

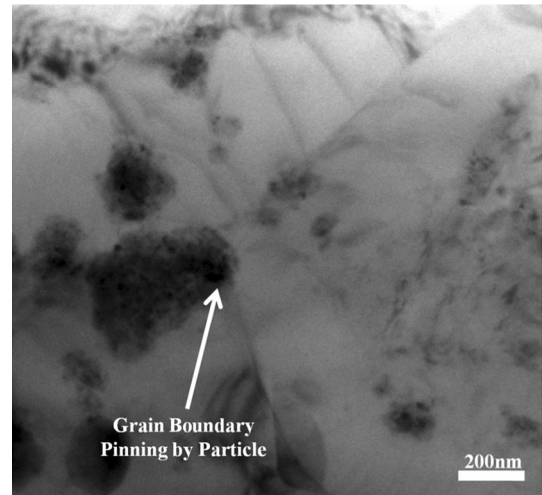


Fig. 12 TEM bright field image of FSPed Al-TiO₂ composite with grain boundary pinned by a particle

$$\Delta\sigma_{\text{orowan}} = \frac{0.13G_m b}{\lambda} \ln \frac{r}{b} \quad (\text{Eq 3})$$

where $\Delta\sigma_{\text{orowan}}$ is the change in yield strength due to the Orowan strengthening by the particles, G_m is the shear modulus of the matrix, b is Burger's vector, λ is inter-particle spacing and r is the radius of the particles. The inter-particle spacing is given by

$$\lambda = d_p \left[\left(\frac{1}{2V_p} \right)^{1/3} - 1 \right] \quad (\text{Eq 4})$$

where, d_p is the diameter of the particle and V_p is the volume fraction of the particle (Ref 39). The Orowan-Ashby equation predicts a yield strength of 94 MPa, and from the tensile test a yield strength of 97 MPa was obtained. The dominant role

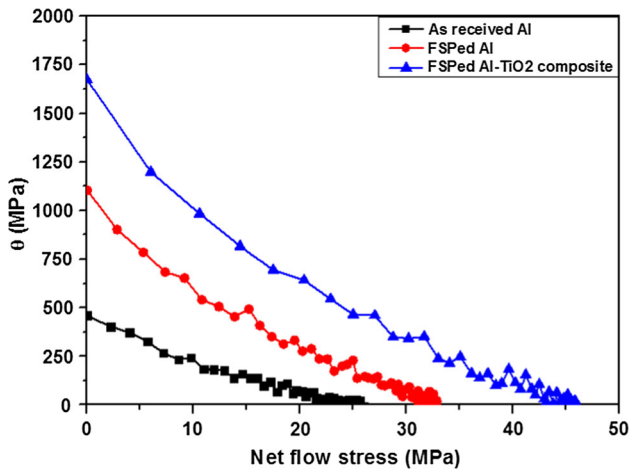


Fig. 13 Work hardening rate (θ) vs. net flow stress curves of as-received CP Al, sixth pass FSPed Al and Al-TiO₂ composite

of Orowan strengthening is confirmed by a TEM image showing the multiple pinned dislocations by a particle (Fig. 11a).

To analyze the effect of reinforcements and FSP on the work-hardening rate, a differential form of the Voces equation $\theta = \theta_o \left(1 - \frac{\sigma}{\sigma_s}\right)$ was used to plot the Kocks-Mecking curves, where θ is the hardening rate, θ_o is the work-hardening limit, σ is the current flow stress and σ_s is the saturation stress [40]. It is seen that that the strain-hardening rate of as-received CP aluminum, FSPed CP aluminum and FSPed Al-TiO₂ composite is 480, 1125 and 1650 MPa, respectively (Fig. 12). It is also seen from Fig. 13 that the FSPed CP aluminum and Al-TiO₂ composites show stage III hardening.

5. Conclusions

In the current study, an Al-TiO₂ composite was synthesized, and its microstructure and mechanical characterization were investigated. From the results, the following conclusions can be drawn:

- The thermo-mechanical action during FSP leads to fracture of TiO₂ particles resulting in their reaction with aluminum matrix. The progression of the reaction during successive passes was confirmed by XRD.
- The grain size refinement of the Al-TiO₂ composite was due to the combined effect of dynamic recrystallization and Zener pinning during FSP.
- The fractographs showed a good interfacial bonding between the matrix and reinforcement, and the fracture was initiated in large un-reacted TiO₂ particle.
- The 26% increase in yield and a 44% increase in UTS were observed due to the combined effect of grain refinement and Orowan strengthening.
- Work-hardening rate increased in Al-TiO₂ composite, and it exhibited stage III hardening.

Acknowledgments

AKP and SVK would like to thank the Advanced Facility for Microscopy and Microanalysis (AFMM) at the Indian Institute of Science, Bengaluru, for providing the facilities. HCM wishes to acknowledge support from the Department of Materials Engineering at the Indian Institute of Science, Bengaluru, to carry out mechanical characterization. This research did not receive any specific grant from funding agencies in the public, commercial or not-for-profit sectors.

References

1. W. Thomas, Friction Stir butt-welding, International Patent Application No. PCT/GB92/0220 (1991)
2. R.S. Mishra and Z. Ma, Friction Stir Welding and Processing, *Mater. Sci. Eng., A*, 2005, **50**(1), p 1–78
3. E.E. Patterson, Y. Hovanski, and D.P. Field, Microstructural Characterization of Friction Stir Welded Aluminum-Steel Joints, *Metall. Mater. Trans. A*, 2016, **47**(6), p 2815–2829
4. L. Ceschini, I. Boromei, G. Minak, A. Morri, and F. Tarterini, Effect of Friction Stir Welding on Microstructure, Tensile and Fatigue Properties of the AA7005/10 vol.% Al₂O₃ Composite, *Compos. Sci. Technol.*, 2007, **67**(3), p 605–661
5. W.B. Lee, C.Y. Lee, M.K. Kim, J.I. Yoon, Y.J. Kim, Y.M. Yoen, and S.B. Jung, Microstructures and Wear Property of Friction Stir Welded AZ91 Mg/SiC Particle Reinforced Composite, *Compos. Sci. Technol.*, 2006, **66**(11), p 1513–1520
6. R.S. Mishra, M. Mahoney, S. McFadden, N. Mara, and A. Mukherjee, High Strain Rate Superplasticity in a Friction Stir Processed 7075 Al Alloys, *Scr. Mater.*, 1999, **42**(2), p 163–168
7. P.B. Berbon, W.H. Bingel, R.S. Mishra, C.C. Bampton, and M.W. Mahoney, Friction Stir Processing: A Tool to Homogenize Nanocomposite Aluminum Alloys, *Scr. Mater.*, 2001, **44**(1), p 61–66
8. Y. Kwon, I. Shigematsu, and N. Saito, Mechanical Properties of Fine-Grained Aluminum Alloy Produced by Friction Stir Process, *Scr. Mater.*, 2003, **49**(8), p 785–789
9. C. Rhodes, M. Mahoney, W. Bingel, and M. Calabrese, Fine-Grain Evolution in Friction-Stir Processed 7050 Aluminum, *Scr. Mater.*, 2003, **48**(10), p 1451–1455
10. Z. Ma, R.S. Mishra, and M.W. Mahoney, Superplasticity in Cast A356 Induced via Friction Stir Processing, *Scr. Mater.*, 2004, **50**(7), p 931–935
11. X.L. Shi, R.S. Mishra, and T.J. Watson, Effect of Temperature and Strain Rate on Tensile Behavior of Ultrafine-Grained Aluminum Alloys, *Mater. Sci. Eng., A*, 2008, **494**(1), p 247–252
12. J.Q. Su, T. Nelson, and C. Sterling, Grain Refinement of Aluminum Alloys by Friction Stir Processing, *Philos. Mag.*, 2006, **86**(1), p 1–24
13. I. Charit and R.S. Mishra, Evaluation of Microstructure and Superplasticity in Friction Stir Processed 5083 Al Alloys, *J. Mater. Res.*, 2004, **19**(11), p 3329–3342
14. P.B. Berbon, W.H. Bingel, R.S. Mishra, C.C. Bampton, and M.W. Mahoney, Friction Stir Processing: A Tool to Homogenize Nanocomposite Aluminum Alloys, *Scr. Mater.*, 2001, **44**(1), p 61–66
15. M. Saadatmand and J.A. Mohandesi, Comparison Between Wear Resistance of Functionally Graded And Homogenous Al-SiC Nanocomposite Produced by Friction Stir Processing (FSP), *J. Mater. Eng. Perform.*, 2014, **23**(3), p 736–742
16. R. Beygi, M.Z. Mehrizi, and G. Eisaabadi B, Friction Stir Processing of Al with Mechanically Alloyed Al-TiO₂-Graphite Powder: Microstructure and Mechanical Properties, *J. Mater. Eng. Perform.*, 2017, **26**(3), p 1455–1462
17. R.S. Mishra, Z. Ma, and I. Charit, Friction Stir Processing: A Novel Technique for Fabrication of Surface Composite, *Mater. Sci. Eng., A*, 2003, **341**(1), p 307–310
18. C. Hsu, P. Kao, and N. Ho, Ultrafine-Grained Al-Al₂ Cu Composite Produced In Situ by Friction Stir Processing, *Scr. Mater.*, 2005, **53**(3), p 341–345
19. C.J. Hsu, C.Y. Chang, P.W. Kao, N.J. Ho, and C.P. Chang, Al-Al₃ Ti Nanocomposites Produced In Situ by Friction Stir Processing, *Acta Mater.*, 2006, **54**(19), p 5241–5249

20. N. Chawla and Y.L. Shen, Mechanical Behaviour of Particle Reinforced Metal Matrix Composites, *Adv. Eng. Mater.*, 2001, **3**(6), p 357–370
21. L. Davis and J. Allison, Residual Stresses and Their Effects on Deformation, *Metall. Mater. Transac. A*, 1993, **24**(11), p 2487–2496
22. M. Vogelsang, R. Arsenault, and R. Fisher, An In Situ HVEM Study of Dislocation Generation at Al/SiC Interfaces in Metal Matrix Composites, *Metall. Mater. Trans. A*, 1986, **17**(3), p 379–389
23. R. Arsenault and S. Wu, A Comparison of PM vs. Melted SiC/Al Composites, *Scr Mater.*, 1988, **22**(6), p 767–772
24. P. Krajewski, J. Allison, and J. Jones, The Influence of Matrix Microstructure and Particle Reinforcement on the Creep Behavior of 2219 Aluminum, *Metall. Mater. Trans. A*, 1993, **24**(1), p 2731–2741
25. K.S. Tun and M. Gupta, Improving Mechanical Properties of Magnesium Using Nano-yttria Reinforcement and Microwave Assisted Powder Metallurgy Method, *Compos. Sci. Technol.*, 2007, **67**(13), p 2657–2664
26. N. Chawla, J. Jones, C. Andres, and J. Allison, Effect of SiC Volume Fraction and Particle Size on the Fatigue Resistance of a 2080 Al/SiCp Composite, *Metall. Mater. Trans. A*, 1998, **29**(11), p 2843–2854
27. F. Hou, W. Wang, and H. Guo, Effect of the Dispersibility of ZrO₂ Nanoparticles in Ni–ZrO₂ Electroplated Nanocomposite Coatings on the Mechanical Properties of Nanocomposite Coatings, *Appl. Surf. Sci.*, 2006, **252**(10), p 3812–3817
28. Q. Zhang, B. Xiao, W. Wang, and Z. Ma, Reactive Mechanism and Mechanical Properties of In Situ Composites Fabricated from an Al–TiO₂ System by Friction Stir Processing, *Acta Mater.*, 2012, **60**(20), p 7090–7103
29. F. Khodabakhshi, A. Simchi, A. Kokabi, M. Sadeghahmadi, and A. Gerlich, Reactive Friction Stir Processing of AA 5052-TiO₂ Nanocomposite: Process-Microstructure-Mechanical Characteristics, *Mater. Sci. Technol.*, 2015, **31**(4), p 426–435
30. F. Khodabakhshi, A. Simchi, A. Kokabi, M. Nosko, F. Simančik, and P. Švec, Microstructure and Texture Development During Friction Stir Processing of Al-Mg Alloy Sheets with TiO₂ Nanoparticles, *Mater. Sci. Eng. A*, 2014, **605**, p 108–118
31. V.C. Gudla, F. Jensen, A. Simar, R. Shabadi, and R. Ambat, Friction Stir Processed Al-TiO₂ Surface Composites: Anodising Behaviour and Optical Appearance, *Appl. Surface Sci.*, 2015, **324**(Supplement C), p 554–562
32. S. Mahshid, M.S. Ghamsari, M. Askari, N. Afshar, and S. Lahuti, Synthesis of TiO₂ Nanoparticles by Hydrolysis and Peptization of Titanium Isopropoxide Solution, *Semicond. Phys. Quan. Electron. Optoelectron.*, 2006, **9**(2), p 65–68
33. K. Jata, S. Semiati, Continuous dynamic recrystallization during friction stir welding of high strength aluminum alloys, DTIC Document, 2000
34. R. Fonda, J. Bingert, and K. Colligan, Development of Grain Structure During Friction Stir Welding, *Scr Mater.*, 2004, **51**(3), p 243–248
35. A. Kumar, R. Raj, and S.V. Kailas, A Novel in-situ Polymer Derived Nano Ceramic MMC by Friction Stir Processing, *Mater. Des.*, 2015, **85**, p 626–634
36. M. Guerra, C. Schmidt, J. McClure, L. Murr, and A. Nunes, Flow Patterns During Friction Stir Welding, *Mater. Charact.*, 2002, **49**(2), p 95–101
37. A. Kumar, D. Yadav, C.S. Perugu, and S.V. Kailas, Influence of Particulate Reinforcement on Microstructure Evolution and Tensile Properties of in-situ Polymer Derived MMC by Friction Stir Processing, *Mater. Des.*, 2017, **113**, p 99–108
38. C. Chang, C. Lee, and J. Huang, Relationship Between Grain Size and Zener-Holloman Parameter During Friction Stir Processing in AZ31 Mg alloys, *Scr Mater.*, 2004, **51**(6), p 509–514
39. Z. Zhang and D. Chen, Consideration of Orowan Strengthening Effect in Particulate-Reinforced Metal Matrix Nanocomposites: A Model for Predicting Their Yield Strength, *Scr Mater.*, 2006, **54**(7), p 1321–1326
40. U. Kocks, Laws for Work Hardening and Low-Temperature Creep, *J. Eng. Mater. Technol.*, 1976, **98**(1), p 76–85